ACS Catalysis

Research Article

pubs.acs.org/acscatalysis

Electrochemical Formation of Reactive Oxygen Species at Pt (111)—A Density Functional Theory Study

Mohammad J. Eslamibidgoli and Michael H. Eikerling*

Department of Chemistry, Simon Fraser University, 8888 University Drive, Burnaby, British Columbia, Canada, V5A 1S6

ABSTRACT: Density functional theory was used to investigate the influence of the Pt adsorption state on the formation of hydrogen peroxide (H_2O_2) and hydroxyl radical ($^{\bullet}OH$) as two important reactive oxygen species. We generated the free energy diagrams of reduction sequences involving O_2 and H_2O_2 as reactants and H_2O_2, $^{\bullet}OH$, or H_2O as products. The Pt (111)−water interface was considered in three adsorption states that are encountered in different regions of the electrode potential: an adsorption state with a monolayer of hydrogen (low electrode potential); a clean surface (intermediate potential); and an adsorption state with 1/3 of a monolayer of oxygen (high potential). Results reveal a strong impact of surface water interactions on the pathways of water oxidation and oxygen reduction reactions. In agreement with experimental results reported in the literature, we found that the oxygen reduction pathway is highly sensitive to the hydrogen coverage. Coverage by one monolayer hydrogen renders the surface highly hydrophobic, thereby suppressing its activity for the oxygen reduction. Therefore, for high hydrogen coverage, the formation of H_2O_2 by a two-electron pathway becomes a preferred path. We discuss results in the context of radical-initiated chemical degradation of polymer electrolyte membranes in polymer electrolyte fuel cells.

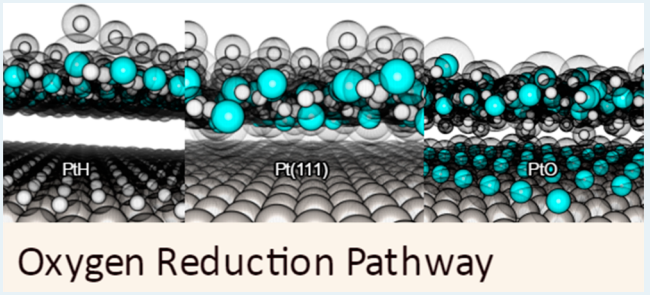

KEYWORDS: *Pt electrocatalysis, surface oxide reactions, Pt-in-the-membrane, PEM degradation, hydrogen peroxide, hydroxyl radical*

1. INTRODUCTION

Platinum catalyzes a plethora of reactions in the chemical industry. Pt-based compounds have also shown promise in medical applications as chemotherapeutic agents to treat neurodegenerative diseases and cancers.[1,2] However, previous studies suggest that Pt-class drugs exhibit dose-dependent cytotoxicity by promoting the production of reactive oxygen species (ROS), such as the superoxide anion radical ($O_2^{\bullet-}$), hydroxyl radical ($^{\bullet}OH$), and hydrogen peroxide (H_2O_2).[3]

In a polymer electrolyte fuel cell (PEFC), solid metal-like deposits of Pt in the polymer electrolyte membrane (PEM), which originate from Pt dissolution in the catalyst layer,[4−7] play an important role in radical-initiated membrane degradation.[8] In the presence of hydrogen and oxygen gas crossover, solid Pt nanodeposits provide catalyst surface sites for reactions involving oxygen radicals.[9,10] In addition, surface reactions at Pt facilitate the decomposition or generation of H_2O_2.[11] In the latter case, H_2O_2 formed at Pt deposits in the PEM can react at metal impurities such as Fe^{2+} and Fe^{3+} to produce $^{\bullet}OH$ (e.g., via Fenton's type reactions).[12] Radicals attack weak bonds of ionomer molecules and chemically degrade the PEM.[13,14]

The balance of competing processes involving the formation or deactivation of ROS at nanodeposits in the PEM depends on the size, shape, and composition of Pt particles or Pt-alloy;[15,16] moreover, it depends on the local thermodynamic conditions and the chemical architecture and self-organized structure of the PEM.[8,17,18] Local electrochemical conditions in the electrolyte medium are functions of pH as well as H_2 and O_2 concentrations, which in turn determine the local particle potential.[10,11,19]

Cyclic voltammetry (CV) studies reveal the Pt surface adsorption state as a function of electrode potential;[20−24] CVs of Pt—be it for nanoparticle-based supported catalysts or extended surfaces—distinguish three characteristic potential regions: (i) the region of hydrogen under-potential deposition (H_{UPD} region) at electrode potentials between 0.05 V < E < 0.40 V vs RHE; (ii) the double layer region at 0.40 V < E < 0.60 V vs RHE and (iii) the surface oxide region at E > 0.7 V vs RHE.

Marković et al.[25,26] studied the oxygen reduction reaction (ORR) on a rotating-disk electrode using Pt low-index single-crystal surfaces. They found that the ORR is highly structure-sensitive in the H_{UPD} region. The activity of the ORR on Pt (111) decreases in this region, reaching half of the value of the diffusion-limited current for the four-electron process; the diffusion-limited current in this potential region corresponds to the two-electron reduction of O_2 with near 100% H_2O_2 formation.[27] Similarly, the H_2O_2 reduction activity was seen to decrease with hydrogen adsorption.[25] The authors discussed that these results imply a change in the mechanism of the ORR in the hydrogen adsorption region. However, in spite of the

Received: June 4, 2015
Revised: August 19, 2015
Published: September 4, 2015

DOI: 10.1021/acscatal.5b01154
ACS Catal. 2015, 5, 6090−6098

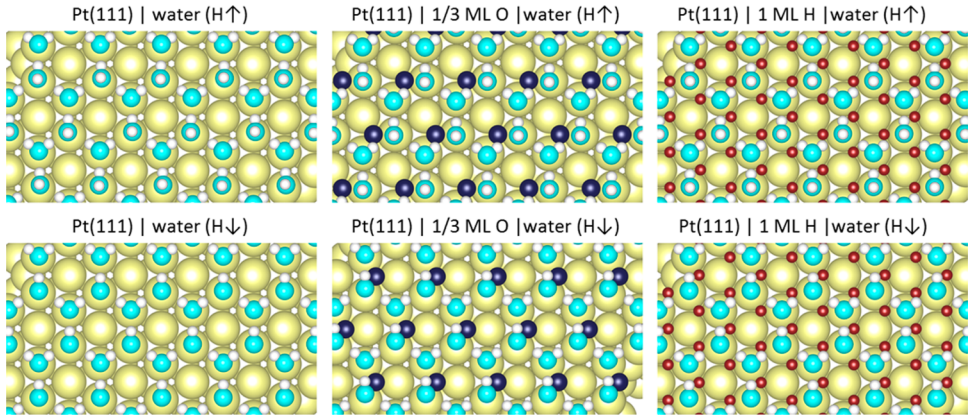

Figure 1. Top view of the final states of the model systems; yellow, light blue, white, brown, and dark blue colors are used to represent Pt, O, H, O*, and H*, respectively.

importance of this process, to the best of our knowledge, it has not yet been theoretically addressed.[28−30]

In an approach to understand the balance of H_2O_2 and $^{\bullet}OH$ at Pt nanodeposits in the PEM, we have recently presented an improved reaction-diffusion model to calculate the local potential at isolated Pt particles in the PEM.[10] The potential depends on the local composition of the electrolyte. Under H_2-rich conditions, the potential is close to the equilibrium potential of the hydrogen oxidation reaction (HOR); while under O_2-rich conditions, it is closer to the equilibrium potential of the ORR. The transition between the two cases occurs at a point in the membrane where both HOR and ORR are controlled by diffusion.[10]

Subsequently, we related the particle potential to specific adsorption states of Pt, using experimental data[31−33] and DFT simulations.[34−38] As a logical continuation, the present article focuses on DFT studies of the reaction paths in different surface adsorption states that correspond to distinct potential regions, discussed in the previous paragraph. We have evaluated processes that lead to formation or deactivation of H_2O_2 and $^{\bullet}OH$ at the Pt-water interface. Our study is different from extensive investigations of ORR at Pt (111),[28,39−42] since we take explicitly into account both adsorbates and a water layer at the surface. We will discuss the significance of our results for reactions at Pt nanodeposits in PEMs, as well as in the broader context of Pt-catalyzed surface reactions.

2. COMPUTATIONAL METHODS

All electronic structure calculations were carried out with the periodic DFT package VASP.[43] The ionic cores were represented by projected augmented waves (PAW).[44] The Kohn−Sham one-electron wave functions were expanded in a plane wave basis set up to an energy cutoff of 400 eV. Exchange−correlation effects were incorporated within the generalized gradient approximation (GGA), using the exchange-correlation functional by Perdew, Burke, and Ernzerhof (PBE).[45] This functional consistently describes the properties of water at metal surfaces.[46−48] Geometry optimization studies were terminated when all forces on ions were less than 0.03 eV $Å^{-1}$. We considered the effect of spin polarization in total energy calculations of hydroxyl radical in the gas phase. Minimum energy structures were determined using Monkhorst−Pack k-point sampling grids with 3 × 3 × 1 k points.[49]

The surface was modeled by a supercell containing a four-layer slab of Pt (111) and a $2\sqrt{3} \times 2\sqrt{3}$-R30° water layer with hexagonal structure on one side of the slab to model the metal-solution interface. The hexagonal water structure at close-packed metal surfaces has been studied experimentally[50,51] and theoretically.[46,52] Our model included 12 Pt atoms per layer of the slab and 8 water molecules per unit cell. Repeated slabs were separated by a vacuum region of 15 Å.

The simulated slab is asymmetric, with adsorbents and water layer considered only at one surface. This configuration leads to the accumulation of equal and opposite charges at opposing surfaces of the slab. A standard dipole correction scheme,[53] implemented in VASP, has been used to compensate the unphysical interaction between opposite surfaces that correspond to neighboring images across the vacuum region of the periodically repeated slab. In this approach, a dipole moment is inserted in the center plane of the vacuum region that results in a constant potential value.

In all geometry optimizations, the two bottom layers of the slab were fixed in their bulk positions, while the two top layers together with adsorbates and the water layer were allowed to relax. It should be noted that at low temperature the arrangement of a monolayer of water at Pt (111) has $\sqrt{37} \times \sqrt{37}$R25.3° and $\sqrt{39} \times \sqrt{39}$R16.1° periodicities,[54] as found in high-resolution STM images[55] and DFT calculations;[56] however, we did not use these larger structures for our investigation.

We set out to study the influence of the surface adsorption state on the energetics of Pt surface reactions; therefore, we considered three adsorption states for Pt (111) that correspond to different potential regions: (1) for the H_{UPD} region, we considered adsorption of one monolayer (ML) of hydrogen at the fcc sites, which has been found theoretically to be more stable compared to adsorption at atop and hcp site;[34−36] (2) in the double layer potential region, we considered an adsorbate-free Pt surface in direct contact with a water overlayer as the most stable surface state;[34,37] for the oxide region, we considered 1/3 of a monolayer of oxygen evenly adsorbed at fcc sites.[34,37,38]

To account for the orientation of water molecules at the interface, we evaluated two water structures: (1) the H-up (H↑) structure, originally proposed by Doering and Madey,[57] in which half of the water molecules bind directly to surface with one lone pair orbital of the oxygen (the so-called flat-lying water molecules), while the other half, i.e. every second water molecule in the adsorbed layer, has OH bonds that point away from the surface; (2) the H-down (H↓) structure has OH

DOI: 10.1021/acscatal.5b01154
ACS Catal. 2015, 5, 6090−6098

Table 1. Reaction Energies of the Elementary Reaction Steps (in eV) at U = 0 V[a]

	Pt -water H↑	Pt-water H↓	Pt-1/3 ML O-water H↑	Pt-1/3 ML O-water H↓	Pt-1 ML H-water H↑	Pt-1 ML H-water H↓
mechanism 1						
$O_2^{gas} + H^+ + e^- \rightarrow OOH^*$	**-0.83**	**-0.80**	−0.36	−0.36	−0.09	−0.06
$OOH^* + H_2O^* \rightarrow 3OH^*$	**-1.63**	**-1.69**	+0.43	+0.12	+1.09	+1.26
$3OH^* + H^+ + e^- \rightarrow 2OH^* + H_2O$	**-0.58**	**-0.51**	−1.19	−0.90	−1.57	−1.32
$2OH^* + H^+ + e^- \rightarrow OH^* + H_2O^*$	**-1.00**	**-1.28**	−2.06	−1.94	−2.40	−2.62
$OH^* + H^+ + e^- \rightarrow H_2O$	**-0.87**	**-0.64**	−1.74	−1.84	−1.95	−2.12
mechanism 2						
$OOH^* + H^+ + e^- \rightarrow O^* + H_2O$	**-2.72**	**-2.78**	**-2.57**	**-2.64**	---	---
$O^* + H^+ + e^- \rightarrow OH^*$	**-0.53**	**-0.75**	**-0.81**	**-0.65**	---	---
$OH^* + H^+ + e^- \rightarrow H_2O$	**-0.84**	**-0.59**	**-1.18**	**-1.27**	---	---
mechanism 3						
$OOH^* + H^+ + e^- \rightarrow H_2O_2^*$	−0.60	−0.79	−1.07	−1.09	**-1.35**	**-1.32**
$H_2O_2^* \rightarrow H_2O_2^{gas}$	0.09	0.26	0.08	0.11	0.11	0.04
$H_2O_2^* \rightarrow 2OH^*$	**-2.07**	**-2.07**	**-0.48**	**-0.65**	0.09	0.01
mechanism 4						
$OOH^* + H_2O \rightarrow 2OH^* + {}^\bullet OH$	1.08	1.09	2.52	2.51	2.83	2.72
mechanism 5						
$H_2O_2^* \rightarrow OH^* + {}^\bullet OH$	0.68	0.61	1.53	1.67	1.78	1.88
mechanism 6						
$2OH^* \rightarrow OH^* + {}^\bullet OH$	2.75	2.68	2.02	2.32	1.68	1.90

[a]The values for the most thermodynamically downhill pathways are in bold.

bonds of every other water molecule oriented toward the surface.[58] The corresponding structures are shown in Figure 1. The orientation of surface water molecules depends on electrode potential, adsorption state, and the total surface charge density; the positively (or negatively) charged surface stabilizes the H↑ (or H↓) structures.[59] Fully self-consistent computations of these dependences are still not computationally feasible. In this article, we compare reaction pathways and energetics obtained for the two interfacial water structures with fixed orientation. Consistent with the study by Schnur and Groß,[46] we found that in all cases the H↓ structures are slightly more stable than H↑ structures (by less than 0.05 eV). We note that in thermodynamic equilibrium the two orientations will be mixed due to thermal reorientation of water molecules.[46,59]

3. RESULTS AND DISCUSSION

Oxygen Reduction Pathways at Pt (111). The ORR is an important and notoriously complex reaction in electrochemistry. First-principles quantum mechanics calculations based on DFT have been established as a first and crucial step in a hierarchy of methods to understand the ORR mechanisms at Pt(111).[39] In spite of extensive efforts in this field, pivotal effects such as the sensitivity of the ORR to the surface adsorption state or implications of surface water interactions on reaction pathways have not been understood in sufficient detail.[39,60,61]

In a complete electrochemical ORR sequence, molecular oxygen needs to be associated with four electrons and protons ($O_2 + 4H^+ + 4e^- \rightarrow 2H_2O$).[62] In the process, electrons lose potential energy by occupying lower energy levels in the water molecules formed. The total Gibbs energy change for all four electrons is −4.92 eV, which corresponds to 1.23 eV per electron. The ORR proceeds at the catalyst surface, where electrons are readily available, at a concentration that is determined by the electronic density of states of the metal. Protons are supplied from the electrolyte, with a concentration determined by the composition of the electrolyte and by the distribution of the electrolyte potential.[63]

The ORR sequence involves surface-adsorbed intermediate species (indicated by a "*") such as surface oxide, O*, hydroxide, OH*, superoxide, OOH*, hydrogen peroxide, $H_2O_2^*$, and water, H_2O^*. To generate the free energy diagrams (FED) for the ORR, explicit determination of the binding energies of the intermediates is required.

In this DFT study, we employed a coupled-proton−electron-transfer (CPET) process, originally proposed by Damjanovic and Brusic,[62] for each of the electrochemical reaction steps. This allowed us to use the original approach developed by Nørskov and co-workers[64] to account for the electrode potential in free energy calculations. In this method, the potential, U, is defined relative to the reversible hydrogen electrode, based on the hydrogen oxidation/evolution reaction ($1/2\ H_2^g \leftrightarrow H^+ + e^-$). We assumed that electrochemical reaction steps proceed via the Eley−Rideal mechanisms, which involves species from the gas phase that react with an adsorbed intermediate.

The adsorption free energy is approximated by

$$\Delta G^{int} \approx \Delta E^{int} - eU \quad (1)$$

which neglects zero point and entropy corrections to the free energy, and does not explicitly account for the effect of the pH. In eq 1, e is the elementary charge and ΔE^{int} is the binding energy of the considered intermediate obtained directly from DFT,

$$\Delta E^{int} = E_{total} + \frac{n}{2}E(H_2^g) - E_{ref} \quad (2)$$

Here, E_{total} is the total energy of an intermediate adsorbed to the substrate; and n = 1, 2, or 3 denotes the electrochemical reaction step for the intermediate. The reference energy, E_{ref}, corresponds to the surface configuration optimized with a complete water bilayer (see Figure 1) and a single water molecule in the gas phase.

DOI: 10.1021/acscatal.5b01154
ACS Catal. 2015, 5, 6090−6098

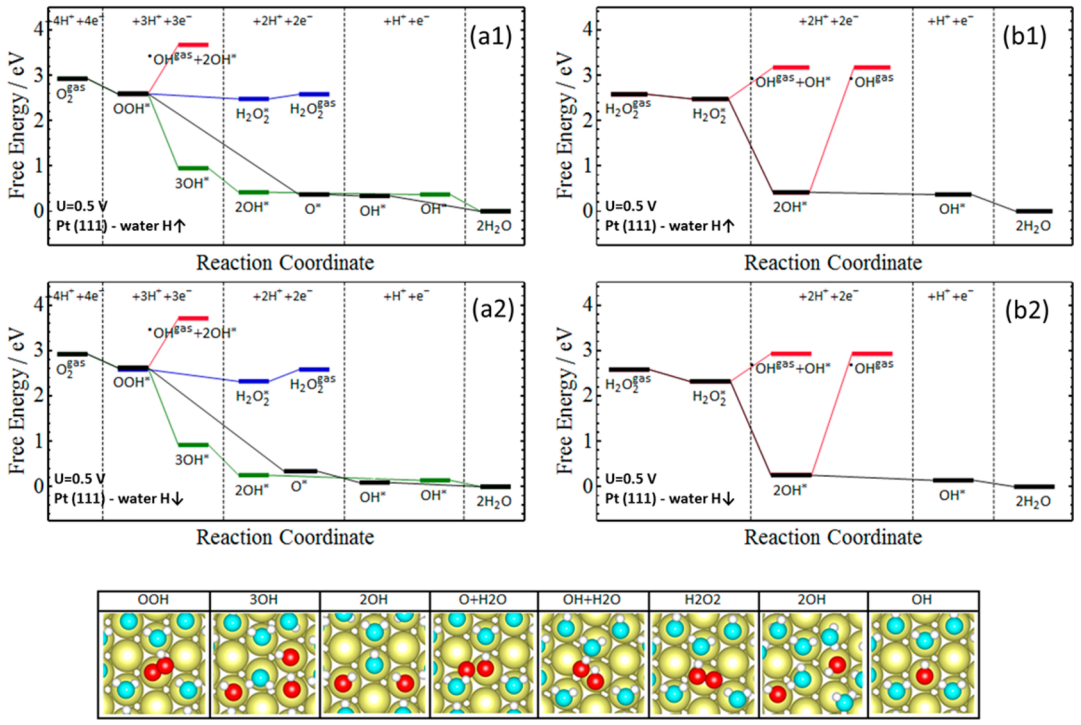

Figure 2. Free energy diagrams of oxygen reduction reaction (on left) and hydrogen peroxide reduction reaction (on right) at clean Pt (111)-water interface for U = 0.5 V vs RHE. Results for H-up and H-down water configurations are shown in top (a1 and b1) and bottom (a2 and b2) panels, respectively. Optimized structures of the most important intermediate states are shown below the energy diagrams. Yellow, light blue and white colors are used to represent Pt, O, and H, respectively; oxygen atoms of the intermediates are shown in red for clarity.

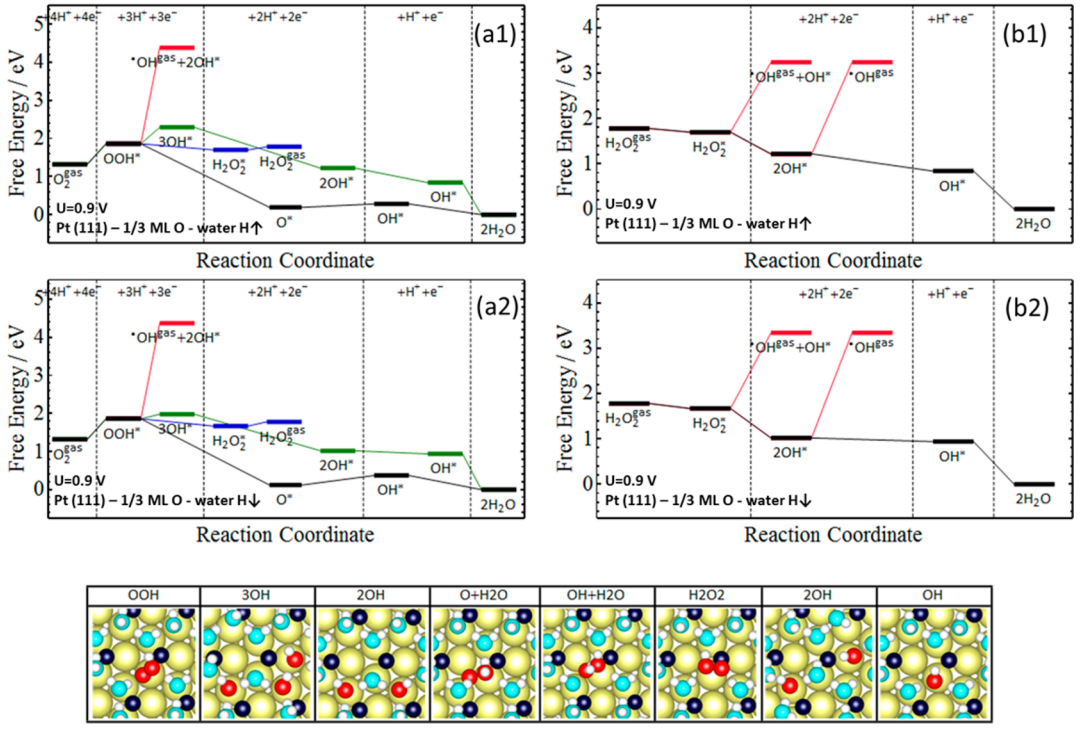

Figure 3. Free energy diagrams of oxygen reduction reaction (on left) and hydrogen peroxide reduction reaction (on right) at 1/3 ML oxygen covered Pt (111)-water interface for U = 0.9 V vs RHE. Results for H-up and H-down water configurations are shown in top (a1 and b1) and bottom (a2 and b2) panels, respectively. Optimized structures of the most important intermediate states are shown below the energy diagrams. Yellow, light blue, and white colors are used to represent Pt, O, and H, respectively; dark blue are adsorbed oxygen atoms and red are oxygen atoms for the intermediates shown in different color for clarity.

We considered three possible mechanisms for the reduction of O_2 to form H_2O or H_2O_2 (M1 to M3), and three mechanisms for the formation of the hydroxyl radical, $^{\bullet}OH$ (M4 to M6):

DOI: 10.1021/acscatal.5b01154
ACS Catal. 2015, 5, 6090−6098

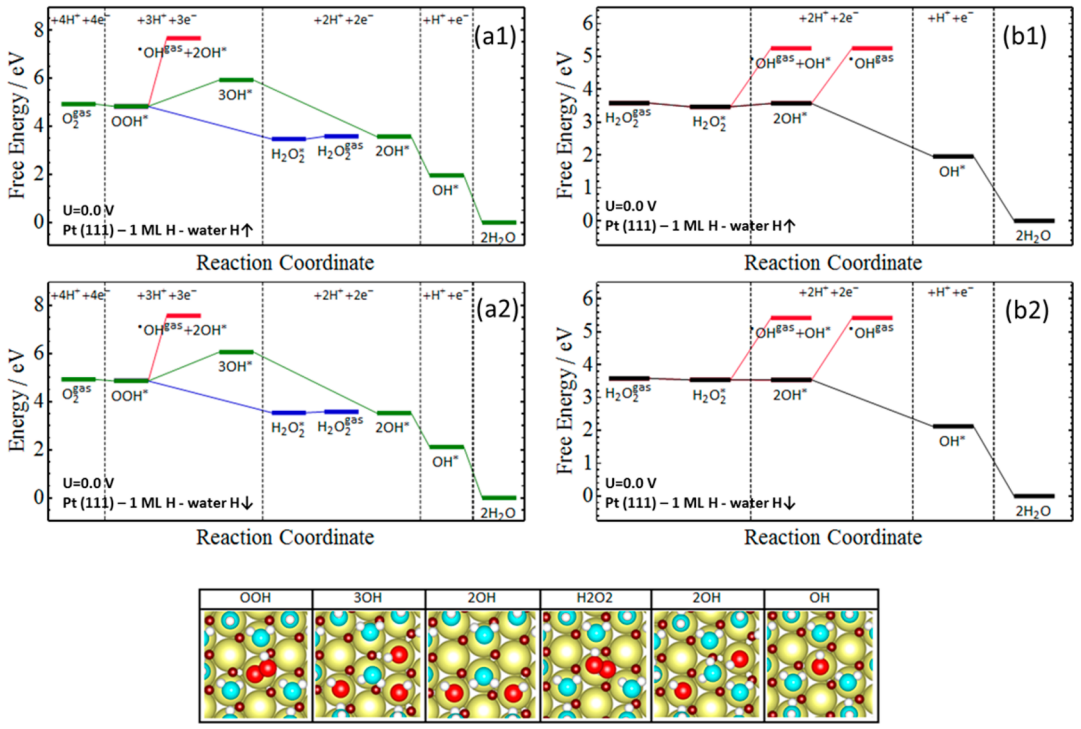

Figure 4. Free energy diagram of oxygen reduction reaction (on left) and hydrogen peroxide reduction reaction (on right) at 1 ML hydrogen-covered Pt (111)-water interface for U = 0 V vs RHE. Results for H-up and H-down water configurations are shown in top (a1 and b1) and bottom (a2 and b2) panels, respectively. Optimized structures of the most important intermediate states are shown below the energy diagram. Yellow, light blue, and white colors are used to represent Pt, O, and H, respectively; brown are adsorbed hydrogen atoms and red are oxygen of the intermediates shown in different color for clarity.

M1. In this mechanism, adsorption of O_2 is followed immediately by one CPET to form OOH*. Then two water molecules at the surface are involved as catalysts to dissociate OOH*, leading to the formation of 3OH* and the immediate reproduction of one water molecule. OH* intermediates undergo three further CPET to reproduce the second water molecule and form two new water molecules as reaction products.

M2. In this mechanism, originally proposed by Anderson et al.,[65,66] OOH* formed in the initial step is converted by a CPET to O* and H_2O*. Then O* undergoes two subsequent CPET to form the second H_2O.

M3. In this mechanism, O_2 adsorption is followed by two CPET to form $H_2O_2^*$. The two-electron reduction pathway is completed when $H_2O_2^*$ desorbs from the surface. However, $H_2O_2^*$ might decompose before desorbing, forming 2OH*, which can undergo two CPET to form two water molecules.

M4. In this mechanism, OOH* formed as in M1, decomposes with water at the surface to form 2OH* and •OH.

M5. H_2O_2 decomposes into OH* and •OH.

M6. •OH is formed by direct desorption of OH*.

Elementary reaction steps of the mechanisms and the corresponding reaction Gibbs energies at U = 0 V versus RHE for the H↑ and H↓ water layer structures are shown in Table 1. Results indicate that the water orientation exerts a smaller impact on the reaction energies than the surface adsorption state. The impact of water orientation on the reaction energies is due to the different surface potential contributions for H↑ and H↓ water layers.[46]

We generated the FED of these mechanisms at the Pt (111)-water interface for the three Pt surface adsorption states defined above. Using binding energies of reaction intermediates obtained from DFT, we calculated the FED for the H_{UPD} region (corresponding to U = 0 V vs RHE), for the double layer region (at U = 0.5 V vs RHE) and for the surface oxide region (U = 0.9 V vs RHE). The open circuit potential for the $4e^-$ ORR was assumed as 1.23 V vs RHE, and that for $2e^-$ ORR was assumed as 0.68 V vs RHE.[67]

Figure 2 (a1 and a2) shows the FEDs for the ORR along the reaction paths M.1 (green path), M.2 (black path), M.3 (blue path for the $2e^-$ reduction), and M.4 (red path) at clean Pt (111), corresponding to U = 0.5 V vs RHE, with H↑ or H↓ water layer structures (upper and lower panels, respectively). Figure 2 (b1 and b2) depicts FEDs for reaction paths M.3 (black) as well as for M.5 and M.6 (in red). The FEDs show that the four-electron pathway of the ORR, resulting in the formation of two water molecules, is clearly preferred for the clean surface state in the intermediate potential region. The formation of H_2O_2 is possible but thermodynamically highly unlikely. Instead, a clean Pt surface could be expected to be highly effective at reducing H_2O_2 to water. The spontaneous formation of •OH is completely insignificant.

Figure 3 (a1 and a2) shows the FEDs of the ORR in the surface oxide region, at U = 0.9 V vs RHE. The increased electrode potential increases the reaction Gibbs energy for the formation of OOH*. In addition, the positive ΔG for the decomposition of OOH* by surface water molecules suggests that M1 is inhibited for this surface state. Similarly, the positive ΔG for H_2O_2 and •OH prevents the formation of these species in the oxide region at U = 0.9 V vs RHE. Instead, H_2O_2 or •OH, if present as a reactant in solution, would be scavenged at the Pt surface and reduced to water in this potential regime, as shown in Figure 3 (b1 and b2). It has also been suggested that the dissociative adsorption of oxygen ($1/2O_2 \rightarrow O^*$) offers a

DOI: 10.1021/acscatal.5b01154
ACS Catal. 2015, 5, 6090−6098

more favorable pathway for the ORR at high electrode potentials;[29,30,68] whereas the formation of OOH* intermediates becomes more favorable as the potential decreases from 0.6 to 0.3 V vs RHE.[30]

Figure 4 (a1 and a2) shows the FEDs of the ORR in the H_{UPD} region, at U = 0.0 V vs RHE. For this surface state, M1 is suppressed, as the intermediate state with formation of 3 OH* involves a high Gibbs energy barrier. M2 is also inhibited for this surface state as the adsorbed hydrogen atoms block the reactive fcc sites necessary for the intermediate formation of O*. However, M3 proceeds spontaneously in this region, because the $2e^-$ process is exothermic at U = 0 V vs RHE. As shown in Figure 4 (b1 and b2), the presence of a monolayer of adsorbed hydrogen prevents HO−OH bond cleavage and stabilizes $H_2O_2^*$ as an intermediate species. Therefore, for this surface state, $H_2O_2^*$ is prevented from further reduction to water by a relatively large energy barrier involved in the formation of 2OH*; instead it is more likely to be released into the electrolyte. In the following section, we will discuss more about this effect in terms of hydrophobicity of the hydrogen-covered Pt (111) surface. Experimental observations of a preferential two-electron exchange in the H_{UPD} region at Pt(111), as well as the detection of H_2O_2 in this potential range confirm our findings.[69−72]

It should be noted that mechanism M1 has been studied by Rossmeisl et al.[73] for a half dissociated hexagonal water structure at Pt (111), where every second water molecule has been oxidized to OH*. They found that O_2 reduction proceeds via a direct $4e^-$ pathway, with negligible peroxide formation.[73] The reaction barrier for proton transfer, calculated in ref 73, was 0.26 eV.

Origin of Hydrogen Peroxide Formation at Hydrogen-Covered Pt (111). Studies using the electrochemical quartz-crystal nanobalance (EQCN) have revealed that the interfacial mass of a Pt electrode reaches a minimum value with the completion of the saturation layer of electroadsorbed H_{upd}.[74] Jerkiewicz et al. discussed that the layer of H_{upd} modifies the surface dipole moment and the wetting properties of Pt, which in turn minimizes the interaction of water molecules with the surface.[74] This renders the hydrogen-covered Pt surface hydrophobic, as has also been conjectured based on a DFT study.[75]

To evaluate the impact of hydrogen adsorption on the surface hydrophobicity, we calculated the average adsorption energy per water molecule at clean and hydrogen-covered surfaces, defined as

$$E^{ads} = \frac{E_{total} - (E_{slab(-H)} + nE_{H_2O})}{n} \quad (3)$$

Here E_{total} is the total energy of the reference system; $E_{slab(-H)}$ is the energy for the slab; E_{H_2O} is the energy of a water molecule in vacuum; and n is the number of water molecules in the unit cell. For a water layer at the surface, we found similar values of E^{ads} = −0.48 eV and −0.46 eV at clean and hydrogen-covered surfaces, respectively, which is consistent with the results of a previous computational study in ref 48.

On the other hand, the adsorption energy for a single flat-lying water molecule (defined as E^{ads}[monomer], where n = 1 in the above equation) was found to be drastically different for clean and hydrogen-covered surfaces. For the clean surface, it was found to be −0.24 eV, and for the hydrogen-covered surface, it was found to be −0.04 eV.

We calculated the H-bond energy in the adsorbed water structure, defined as[76]

$$E^{HB} = (E^{ads}[\text{monomer}]N_{Pt-H_2O} - nE^{ads})/N_{HB} \quad (4)$$

Here, N_{Pt-H2O} is the number of molecule−surface bonds and N_{HB} is the number of H-bonds in the water structure. In this case, we obtained E^{HB} values of −0.15 eV and −0.29 eV for the clean and hydrogen-covered surfaces, respectively. At the hydrogen-covered Pt surface, HB among water molecules are stronger as compared to the clean surface; this is consistent with the finding of weaker adsorption energy for a single flat-lying water molecule at the hydrogen-covered surface.

In Figure 5, the isodensity contours of the total electron density as well as the charge density difference isosurfaces of a water monomer at clean and hydrogen-covered surfaces are compared. As shown, the electron density is small in the region between water molecule and hydrogen-covered surface. Moreover, the distance between water molecule and Pt surface is significantly larger in this case (3.55 Å at hydrogen-covered surface as compared to 2.46 Å at clean surface). Similarly, in the case of one water layer at the surface, the average distance of water molecules from the hydrogen-covered surface was found to be 4.09 Å (and 3.90 Å) in a H↑ (and H↓) structures, whereas the distance from clean surface was obtained as 3.36 Å (and 3.64 Å), respectively.

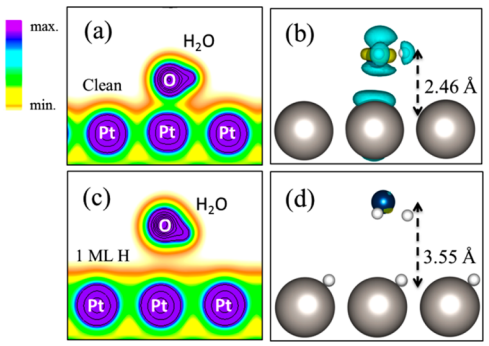

Figure 5. Isodensity contours for the total electron density (left panel) and the three-dimensional charge density differences (right panel) for a water monomer at clean ((a) and (b)), and hydrogen-covered Pt (111) ((c) and (d)), respectively. In (b) and (d), the isosurface value is taken as 0.002 e per $Å^{-3}$.

Figure 6 shows the difference between the total plane-averaged charge density of the interfacial system and separately calculated charge densities of the Pt slab and the adsorbates (defined as $\Delta\lambda$) as a function of Z-coordinate (normal to the

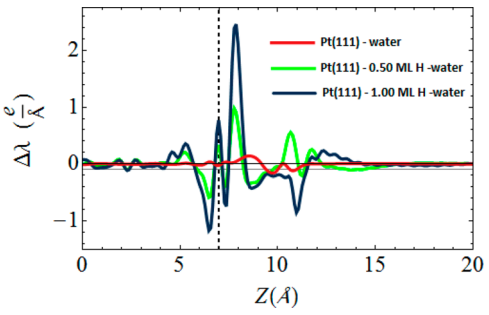

Figure 6. Planar average of the induced charge density along the surface normal for clean and hydrogen-covered surfaces.

DOI: 10.1021/acscatal.5b01154
ACS Catal. 2015, 5, 6090−6098

Table 2. Bader Analysis of Surface Charge (in Units of an Electron, e) for the Electro-Adsorbed Hydrogen Atoms and the Top Two Pt Layers of the (111) Surfaces[a]

	Pt-water	Pt-1/4 ML H-water	Pt-1/2 ML H-water	Pt-3/4 ML H-water	Pt-1 ML H-water
average charge on adsorbed hydrogen atoms on surface (e)	---	−0.046	−0.056	−0.036	−0.028
average charge on 1st top Pt layer (e)	−0.043	−0.019	+0.011	+0.021	+0.034
average charge on 2nd top Pt layer (e)	+0.044	+0.034	+0.022	+0.010	+0.001
dipole moment (e Å)	+0.00189	−0.02259	−0.05796	−0.11991	−0.21181
average distance of water molecules from surface (Å)	3.36	3.55	3.82	4.08	4.09

[a]The charge is reported relative to the corresponding uncharged atom. Values of total dipole moment for the structures without water layer are shown. The average distance (Å) of water molecules in the water layer from the surface is also included for varying hydrogen coverages.

surface). Results reveal that the adsorption of hydrogen induces a large polarization at the interface with the dipole moment directed toward the surface, which is consistent with experimental findings reported in ref 74.

To obtain a more quantitative picture of surface charging effects, we performed Bader analyses[77,78] for various hydrogen coverages. The results are summarized in Table 2. The values represent the partial charge excess/deficiency at adsorbed hydrogen atoms as well as the average charge per Pt atom for the first and for the second layer of the slab. The average charge per Pt atom in the first layer, changes sign from a negative value in the clean surface state to increasingly more positive values with increasing hydrogen coverage. This effect induces a dipole moment at the surface with its direction toward the surface. Values reported on line 4 of Table 2 represent a dipole correction value due to the formation of H_{upd} species. We speculate that the net (or "effective") surface dipole moment will decrease as a result of this dipole correction, weakening the interactions of hydrogen-covered surface with near-surface water molecules. A more detailed analysis of surface charging effects in different adsorption regimes is underway which is beyond the scope of this article.

Impact of Surface Hydrophobicity on Formation of OH*. As discussed in the previous section, adsorbed hydrogen on fcc sites of Pt (111) inhibits the breaking of the O−O bond necessary for the $4e^-$ pathway M2, in which O* is an intermediate. Even though H_2O_2 is a higher energy product than H_2O, a two-electron pathway to produce H_2O_2 is preferred. Uphill reaction steps involved in the dissociation of OOH* to 3OH* (in M1) and the $H_2O_2^*$ decomposition to 2OH* (in M3) render H_2O_2 a relatively stable intermediate reaction product; its diffusion-induced dilution in the electrolyte will suppress the further reaction to H_2O.

As OH* is the key intermediate to understand the path selectivity of the oxygen reduction and hydrogen peroxide decomposition at hydrogen-covered Pt (111), it is useful to generate the surface charge density difference of a system, which contains chemisorbed OH. This gives information about charge transfer and bond formation. It clarifies, moreover, the strength of the interaction between Pt surface and species in the water layer. The charge density difference function for this system is defined as

$$\Delta\rho = \rho_{total} - \rho_{slab(-H)} - \rho_{water-OH} \quad (5)$$

Here ρ_{total} is the charge density of the system; $\rho_{slab(-H)}$ is the charge density for clean (and hydrogen-covered) slab; and $\rho_{water-OH}$ is that for OH in the water layer.

Three-dimensional charge density difference isosurfaces of the clean and hydrogen-covered systems for the H↑ and H↓ structures are shown in Figure 7. The charge accumulation zones (positive $\Delta\rho$), shown in yellow, are caused by electron

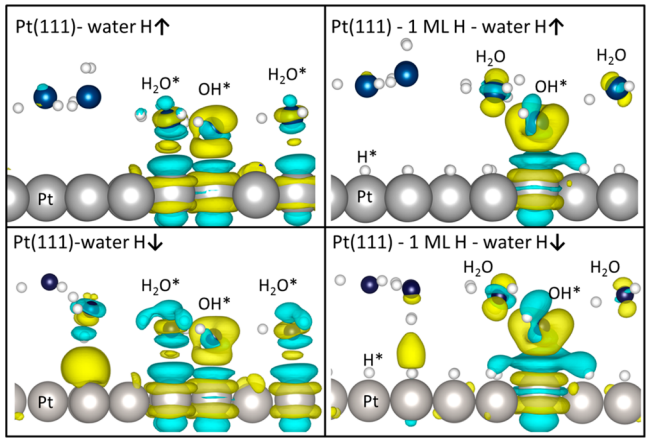

Figure 7. Charge density difference isosurfaces of chemisorbed OH at Pt (111), for clean surface (on left, H-up top, H-down bottom) and for 1 ML hydrogen-covered surface (on right, H-up top, H-down bottom). Yellow shows positive isosurfaces (charge accumulation zones); blue shows negative isosurfaces (charge depletion zones); gray, dark blue, and white show Pt, O and H atoms, respectively. The isosurfaces value is taken as 0.002 e per $Å^{-3}$.

transfer of adsorbed surface species, filling the orbitals close to the Fermi level of the metal. This leads to the charge depletion zones (negative $\Delta\rho$), shown in blue, inducing a local polarization.

Results indicate that the relatively strong interaction between flat-lying water molecules (H-bonded to OH*) and the clean surface facilitates the formation of H_2O−Pt bond. On the other hand, at the hydrogen-covered surface, there is almost no charge transfer between near-surface water molecules and the surface. Indeed, this electrostatic effect is caused by the surface hydrophobicity in the H_{upd} region, which renders the formation of OH* energetically unfavorable. As a result, the decomposition of H_2O_2 to form 2OH* is inhibited in the H_{upd} region but highly favorable at the clean surface. Similarly, the decomposition of OOH* to 3OH*, catalyzed by surface water molecules, becomes highly unfavorable at a hydrogen-covered surface, but a highly favorable process at a clean surface. This interpretation is consistent with our binding energy calculations.

Moreover, we generated the FED of M1 as a function of hydrogen coverage. The $4e^-$ and the $2e^-$ pathways of the ORR are compared in Figure 8 at $U = 0$ V vs RHE. As can be seen, at hydrogen coverage below 1/4 ML, OOH* dissociation to 3OH* becomes an energetically preferred step in comparison to H_2O_2* formation. As the hydrogen coverage increases, the dissociation of OOH* by neighboring surface water molecules is suppressed thereby enhancing the selectivity of the process to H_2O_2 formation.

DOI: 10.1021/acscatal.5b01154
ACS Catal. 2015, 5, 6090−6098

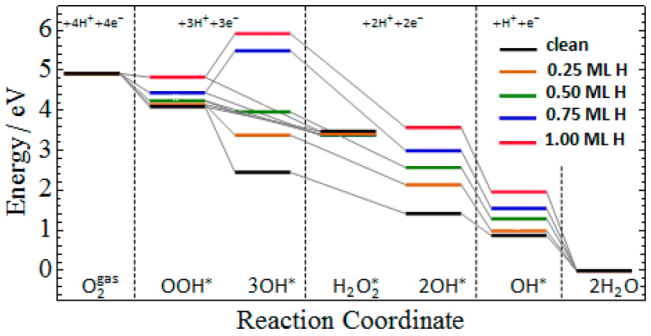

Figure 8. Free energy diagram of oxygen reduction reaction at Pt (111) as a function of hydrogen coverage.

Importance for Fuel Cell Reactions. It has been suggested by several groups that Pt nanodeposits in PEM, originating from Pt dissolution in the catalyst layer, initiate membrane chemical degradation.[8] Ghassemzadeh et al.[79] have observed that the chemical degradation rate was higher in the presence of Pt catalyst for a H_2-rich mixture of H_2 and O_2 (90% H_2, 2% O_2, 8% Ar) as compared to an O_2 -rich mixture (20% O_2, 2% H_2, 78% Ar). Ohguri et al.[9] have detected $^{\bullet}$OH in the presence of Pt particles at both the anode and the cathode sides of the membrane, but the amount is much larger for the anode side. A similar trend was also reported by Aoki et al.[80]

Our results suggest that Pt nanodeposits present in the H_2-rich region of a PEM could be responsible for the formation of H_2O_2. The H_2O_2 released from Pt in H_{UPD} surface configuration could react with iron impurities (Fe^{2+}/Fe^{3+}), which are inevitably present in the membrane,[11,81,82] to form $^{\bullet}$OH and thereby initiate membrane chemical degradation.[13] In addition, our studies show that spontaneous formation of $^{\bullet}$OH at Pt nanodeposits is unlikely. It can be expected that Pt deposits will act as scavengers for $^{\bullet}$OH, which has also been reported experimentally.[83]

Pt nanodeposits under O_2-rich conditions, on the other hand, possess a catalase-like activity to decompose H_2O_2 and produce H_2O.[61] Indeed, it has been recently reported that a Pt band in the PEM, formed close to the cathode catalyst layer, enhances membrane durability.[84]

4. CONCLUSION

Understanding the impact of Pt nanoparticles on the formation/deactivation of ROS in an electrolyte involves a complex phenomenology of local conditions and structure of the electrolyte, as well as structure-dependent transport and reaction processes at solid Pt deposits. In this article, we presented DFT calculations of surface reactions that are involved in the formation/deactivation of two important ROS, namely, H_2O_2 and $^{\bullet}$OH at a Pt (111) surface. We distinguished three adsorption regimes, which are discernible in the cyclic voltammograms that span the appropriate potential range of Pt based catalysts. Results demonstrate that in the H_{upd} potential region the rate of the 2 e^- reduction of O_2 to H_2O_2 is strongly enhanced due to effective inhibition of the 4 e^- ORR. In this region, the metal surface is found to be strongly hydrophobic, in agreement with findings reported earlier by experimentalists. We also found that solid deposits of Pt will always tend to scavenge $^{\bullet}$OH. In addition, if present in the solution due to external sources, H_2O_2 will be decomposed at clean or partially oxide covered surfaces but not at the hydrogen-covered surface. This effect is caused by surface hydrophobicity in this region and weaker interaction of water molecules with the surface, rendering the formation of chemisorbed OH thermodynamically unfavorable.

AUTHOR INFORMATION

Corresponding Author

*E-mail: meikerl@sfu.ca.

Notes

The authors declare no competing financial interest.

ACKNOWLEDGMENTS

This work was funded by an Automotive Partnership of Canada (APC) project on "Next Generation Heavy Duty Fuel Cell Buses (APC-HDFC)", which received excellent support from Ballard Power Systems. Furthermore, the authors wish to acknowledge useful discussions with Dr. A. Roudgar and Dr. A. Malek.

REFERENCES

(1) Kelland, L. *Nat. Rev. Cancer* **2007**, *7*, 573−584.
(2) Reedijk, J. *Chem. Commun.* **1996**, 801−806.
(3) Yao, X.; Panichpisal, K.; Kurtzman, N.; Nugent, K. *Am. J. Med. Sci.* **2007**, *334*, 115−124.
(4) Ferreira, P. J.; la O', G. J.; Shao-Horn, Y.; Morgan, D.; Makharia, R.; Kocha, S.; Gasteiger, H. a. *J. Electrochem. Soc.* **2005**, *152*, A2256−A2271.
(5) Rinaldo, S. G.; Stumper, J.; Eikerling, M. *J. Phys. Chem. C* **2010**, *114*, 5773−5785.
(6) Rinaldo, S. G.; Lee, W.; Stumper, J.; Eikerling, M. *Phys. Rev. E* **2012**, *86*, 041601.
(7) Rinaldo, S. G.; Urchaga, P.; Hu, J.; Lee, W.; Stumper, J.; Rice, C.; Eikerling, M. *Phys. Chem. Chem. Phys.* **2014**, *16*, 26876−26886.
(8) Rodgers, M. P.; Bonville, L. J.; Kunz, H. R.; Slattery, D. K.; Fenton, J. M. *Chem. Rev.* **2012**, *112*, 6075−6103.
(9) Ohguri, N.; Nosaka, A. Y.; Nosaka, Y. *J. Power Sources* **2010**, *195*, 4647−4652.
(10) Eslamibidgoli, M. J.; Melchy, P.-É. A.; Eikerling, M. H. *Phys. Chem. Chem. Phys.* **2015**, *17*, 9802−9811.
(11) Liu, W.; Zuckerbrod, D. *J. Electrochem. Soc.* **2005**, *152*, A1165−A1170.
(12) Borup, R.; Meyers, J.; Pivovar, B.; Kim, Y. S.; Mukundan, R.; Garland, N.; Myers, D.; Wilson, M.; Garzon, F.; Wood, D.; Zelenay, P.; More, K.; Stroh, K.; Zawodzinski, T.; Boncella, J.; McGrath, J. E.; Inaba, M.; Miyatake, K.; Hori, M.; Ota, K.; Ogumi, Z.; Miyata, S.; Nishikata, A.; Siroma, Z.; Uchimoto, Y.; Yasuda, K.; Kimijima, K.-I.; Iwashita, N. *Chem. Rev.* **2007**, *107*, 3904−3951.
(13) Gubler, L.; Dockheer, S. M.; Koppenol, W. H. *J. Electrochem. Soc.* **2011**, *158*, B755−B769.
(14) Ghelichi, M.; Melchy, P. É. A.; Eikerling, M. H. *J. Phys. Chem. B* **2014**, *118*, 11375−11386.
(15) Xia, T.; Kovochich, M.; Brant, J.; Hotze, M.; Sempf, J.; Oberley, T.; Sioutas, C.; Yeh, J. I.; Wiesner, M. R.; Nel, A. E. *Nano Lett.* **2006**, *6*, 1794−1807.
(16) Chen, S.; Kucernak, A. *J. Phys. Chem. B* **2004**, *108*, 13984−13994.
(17) De Bruijn, F. a.; Dam, V. a. T.; Janssen, G. J. M. *Fuel Cells* **2008**, *8*, 3−22.
(18) Liu, Y.; Wu, H.; Li, M.; Yin, J.-J.; Nie, Z. *Nanoscale* **2014**, *6*, 11904−11910.
(19) Takaichi, S.; Uchida, H.; Watanabe, M. *Electrochem. Commun.* **2007**, *9*, 1975−1979.
(20) Biegler, T.; Rand, D. A. J.; Woods, R. *J. Electroanal. Chem. Interfacial Electrochem.* **1971**, *29*, 269−277.
(21) Rand, D. A. J.; Woods, R. *J. Electroanal. Chem. Interfacial Electrochem.* **1972**, *35*, 209−218.
(22) Jerkiewicz, G. *Prog. Surf. Sci.* **1998**, *57*, 137−186.
(23) Jerkiewicz, G. *J. Electrochem. Soc.* **1996**, *143*, 1240−1248.

DOI: 10.1021/acscatal.5b01154
ACS Catal. 2015, 5, 6090−6098

(24) Jerkiewicz, G.; Vatankhah, G.; Lessard, J.; Soriaga, M. P.; Park, Y. S. *Electrochim. Acta* **2004**, *49*, 1451−1459.
(25) Marković, N. M.; Gasteiger, H. A.; Ross, P. N. *J. Phys. Chem.* **1995**, *99*, 3411−3415.
(26) Stamenkovic, V.; Marković, N. M.; Ross, P. N. *J. Electroanal. Chem.* **2001**, *500*, 44−51.
(27) Schmidt, T. J.; Stamenkovic, V.; Ross, P. N.; Marković, N. M. *Fuel Cells* **2001**, *1*, 105−116.
(28) Panchenko, a.; Koper, M. T. M.; Shubina, T. E.; Mitchell, S. J.; Roduner, E. *J. Electrochem. Soc.* **2004**, *151*, A2016−A2027.
(29) Keith, J. A.; Jacob, T. *Angew. Chem., Int. Ed.* **2010**, *49*, 9521−9525.
(30) Markiewicz, M.; Zalitis, C.; Kucernak, A. *Electrochim. Acta* **2015**, DOI: 10.1016/j.electacta.2015.04.066.
(31) Schmidt, T. J.; Ross, P. N.; Marković, N. M. *J. Electroanal. Chem.* **2002**, *524-525*, 252−260.
(32) Marković, N. *Surf. Sci. Rep.* **2002**, *45*, 117−229.
(33) Wakisaka, M.; Suzuki, H.; Mitsui, S.; Uchida, H.; Watanabe, M. *Langmuir* **2009**, *25*, 1897−1900.
(34) Rossmeisl, J.; Nørskov, J. K.; Taylor, C. D.; Janik, M. J.; Neurock, M. *J. Phys. Chem. B* **2006**, *110*, 21833−21839.
(35) Schnur, S.; Groß, A. *Catal. Today* **2011**, *165*, 129−137.
(36) Skúlason, E.; Karlberg, G. S.; Rossmeisl, J.; Bligaard, T.; Greeley, J.; Jónsson, H.; Nørskov, J. K. *Phys. Chem. Chem. Phys.* **2007**, *9*, 3241−3250.
(37) Hansen, H. A.; Rossmeisl, J.; Nørskov, J. K. *Phys. Chem. Chem. Phys.* **2008**, *10*, 3722−3730.
(38) Bondarenko, A. S.; Stephens, I. E. L.; Hansen, H. A.; Pérez-Alonso, F. J.; Tripkovic, V.; Johansson, T. P.; Rossmeisl, J.; Nørskov, J. K.; Chorkendorff, I. *Langmuir* **2011**, *27*, 2058−2066.
(39) Calle-Vallejo, F.; Koper, M. T. M. *Electrochim. Acta* **2012**, *84*, 3−11.
(40) Jacob, T. *Fuel Cells* **2006**, *6*, 159−181.
(41) Yu, T. H.; Sha, Y.; Liu, W. G.; Merinov, B. V.; Shirvanian, P.; Goddard, W. A. *J. Am. Chem. Soc.* **2011**, *133*, 19857−19863.
(42) Keith, J. A.; Jerkiewicz, G.; Jacob, T. *ChemPhysChem* **2010**, *11*, 2779−2794.
(43) Kresse, G.; Furthmüller, J. *Phys. Rev. B: Condens. Matter Mater. Phys.* **1996**, *54*, 11169−11186.
(44) Blöchl, P. E. *Phys. Rev. B: Condens. Matter Mater. Phys.* **1994**, *50*, 17953−17979.
(45) Perdew, J.; Burke, K.; Ernzerhof, M. *Phys. Rev. Lett.* **1996**, *77*, 3865−3868.
(46) Schnur, S.; Groß, A. *New J. Phys.* **2009**, *11*, 125003.
(47) Tonigold, K.; Groß, A. *J. Comput. Chem.* **2012**, *33*, 695−701.
(48) Roman, T.; Groß, A. *Catal. Today* **2013**, *202*, 183−190.
(49) Pack, J. D.; Monkhorst, H. J. *Phys. Rev. B* **1977**, *16*, 1748−1749.
(50) Thiel, P. A.; Madey, T. E. *Surf. Sci. Rep.* **1987**, *7*, 211−385.
(51) Henderson, M. *Surf. Sci. Rep.* **2002**, *46*, 1−308.
(52) Rossmeisl, J.; Skúlason, E.; Björketun, M. E.; Tripkovic, V.; Nørskov, J. K. *Chem. Phys. Lett.* **2008**, *466*, 68−71.
(53) Neugebauer, J.; Scheffler, M. *Phys. Rev. B: Condens. Matter Mater. Phys.* **1992**, *46*, 16067.
(54) Glebov, A.; Graham, A. P.; Menzel, A.; Toennies, J. P. *J. Chem. Phys.* **1997**, *106*, 9382−9385.
(55) Nie, S.; Feibelman, P. J.; Bartelt, N. C.; Thürmer, K. *Phys. Rev. Lett.* **2010**, *105*, 026102.
(56) Feibelman, P. J.; Bartelt, N. C.; Nie, S.; Thürmer, K. *J. Chem. Phys.* **2010**, *133*, 154703.
(57) Doering, D.; Madey, T. *Surf. Sci.* **1982**, *123*, 305−337.
(58) Ogasawara, H.; Brena, B.; Nordlund, D.; Nyberg, M.; Pelmenschikov, A.; Pettersson, L. G. M.; Nilsson, A. *Phys. Rev. Lett.* **2002**, *89*, 276102.
(59) Filhol, J. S.; Doublet, M. L. *Catal. Today* **2013**, *202*, 87−97.
(60) Casalongue, H. S.; Kaya, S.; Viswanathan, V.; Miller, D. J.; Friebel, D.; Hansen, H. A.; Norskov, J. K.; Nilsson, A.; Ogasawara, H. *Nat. Commun.* **2013**, *4*, 2817.
(61) Katsounaros, I.; Schneider, W. B.; Meier, J. C.; Benedikt, U.; Biedermann, P. U.; Auer, A. A.; Mayrhofer, K. J. J. *Phys. Chem. Chem. Phys.* **2012**, *14*, 7384−7391.
(62) Damjanovic, A.; Brusic, V. *Electrochim. Acta* **1967**, *12*, 615−628.
(63) Eikerling, M.; Kulikovsky, A. *Polymer Electrolyte Fuel Cells: Physical Principles of Materials and Operation*; CRC Press: Boca Raton, FL, 2014; pp 194−212.
(64) Nørskov, J. K.; Rossmeisl, J.; Logadottir, A.; Lindqvist, L.; Kitchin, J. R.; Bligaard, T.; Jónsson, H. *J. Phys. Chem. B* **2004**, *108*, 17886−17892.
(65) Anderson, A. B.; Albu, T. V. *J. Electrochem. Soc.* **2000**, *147*, 4229−4238.
(66) Sidik, R. a.; Anderson, A. B. *J. Electroanal. Chem.* **2002**, *528*, 69−76.
(67) Hoare, J. P. *The Electrochemistry of oxygen*; Interscience Publishers: London, 1968; pp 64−68.
(68) Wang, J. X.; Zhang, J.; Adzic, R. R. *J. Phys. Chem. A* **2007**, *111*, 12702−12710.
(69) Marković, N. M.; Gasteiger, H. A.; Ross, P. N. *J. Phys. Chem.* **1995**, *99*, 3411−3415.
(70) Marković, N. M.; Gasteiger, H.; Ross, P. N. *J. Electrochem. Soc.* **1997**, *144*, 1591−1597.
(71) Gómez-Marín, A. M.; Schouten, K. J. P.; Koper, M. T. M.; Feliu, J. M. *Electrochem. Commun.* **2012**, *22*, 153−156.
(72) Kuzume, A.; Herrero, E.; Feliu, J. M. *J. Electroanal. Chem.* **2007**, *599*, 333−343.
(73) Tripković, V.; Skúlason, E.; Siahrostami, S.; Nørskov, J. K.; Rossmeisl, J. *Electrochim. Acta* **2010**, *55*, 7975−7981.
(74) Jerkiewicz, G.; Vatankhah, G.; Tanaka, S. I.; Lessard, J. *Langmuir* **2011**, *27*, 4220−4226.
(75) Roman, T.; Groß, A. *Catal. Today* **2013**, *202*, 183−190.
(76) Meng, S.; Wang, E. G.; Gao, S. W. *J. Chem. Phys.* **2003**, *119*, 7617−7620.
(77) Bader, R. F. W. *Atoms in Molecules - A Quantum Theory*; Oxford University Press: New York, 1990.
(78) Henkelman, G.; Arnaldsson, A.; Jónsson, H. *Comput. Mater. Sci.* **2006**, *36*, 354−360.
(79) Ghassemzadeh, L.; Kreuer, K. D.; Maier, J.; Müller, K. *J. Phys. Chem. C* **2010**, *114*, 14635−14645.
(80) Aoki, M.; Uchida, H.; Watanabe, M. *Electrochem. Commun.* **2006**, *8*, 1509−1513.
(81) Mittal, V. O.; Kunz, H. R.; Fenton, J. M. *J. Electrochem. Soc.* **2007**, *154*, B652−B656.
(82) Pozio, A.; Silva, R. F.; De Francesco, M.; Giorgi, L. *Electrochim. Acta* **2003**, *48*, 1543−1549.
(83) Hamasaki, T.; Kashiwagi, T.; Imada, T.; Nakamichi, N.; Aramaki, S.; Toh, K.; Morisawa, S.; Shimakoshi, H.; Hisaeda, Y.; Shirahata, S. *Langmuir* **2008**, *24*, 7354−7364.
(84) Macauley, N.; Ghassemzadeh, L.; Lim, C.; Watson, M.; Kolodziej, J.; Lauritzen, M.; Holdcroft, S.; Kjeang, E. *ECS Electrochem. Lett.* **2013**, *2*, F33−F35.

DOI: 10.1021/acscatal.5b01154
ACS Catal. 2015, 5, 6090−6098